Design of Bone Scaffolds Structures for Rapid Prototyping with Increased Strength and Osteoconductivity

Marcin Lipowiecki, Dermot Brabazon,
School of Mechanical and Manufacturing Engineering, Dublin City University, Ireland

Abstract.

The geometry of bone scaffolds plays a crucial role in bone tissue regeneration. This architecture, especially pore size and shape, determines the mechanical strength of the scaffold. A number of previous workers have indicated the parameters which are believed to be the main stimulus in the adaptive bone remodelling process. An ideal bone manufacturing system would deliver bone morphogenetic proteins (BMP) and provide adequate mechanical properties. The aim of this study was to design a highly osteoconductive and mechanically strong bone regeneration scaffold which can be successfully manufactured. Three porous architectures of scaffold were designed using Solid Edge^{TM} 3D solid modelling software. The equivalent trabecular structure model consisted of repeatable unit cells arranged in layers to fill the chosen scaffold volume. The three different unit cell structures examined include cubic, triangular, and hexagonal polyhedral. Designed scaffold's pores were varied in this study to 120, 340 and 600μm. This range was selected to meet one of the requirements of the scaffold design — the macropores must be at least 100μm in diameter, so the cells can penetrate and proliferate within the structure. The strengths of each scaffold were determined using ANSYS^{TM} finite element software. Trabecular scaffold designs were analysed independently and in connection with simulated cortical bone in order to investigate their stress-strain response. As well as providing useful information on strengths developed from these topologies, the models developed indicated geometric constraints in order to tailor scaffolds to specific patient needs.

Keywords: Bone Scaffold, Rapid Prototyping, Porosity, Osteoconductivity.

Introduction

To date, autograft (tissue transplanted from one part of the body to another in the same individual) and allograft (the transplant of an organ or tissue from one individual to another of the same species) treatments for bone loss have achieved varying degrees of success in restoring form and function and can carry significant risks. An attractive alternative to natural bone grafts is a synthetic scaffold that is biocompatible, osteoconductive, and able to withstand mechanical loading. The geometry of the scaffolds plays a crucial role in bone tissue regeneration. A number of workers have indicated the parameters (e.g. pore size and geometry, rod and plates orientation, and material properties) which are believed to be the main stimulus in adaptive bone remodelling process [1-6]. The primary roles of scaffold are to serve as an adhesion substrate for cells, facilitate the localisation and delivery of cells when implanted, and provide temporary mechanical support to the newly grown tissue by defining and maintaining a 3D structure [7]. A successful bone scaffold should possess an open-pore geometry with a highly porous surface and microstructure that enables cell

ingrowth [8-10]. A recent study revealed that the scaffolds' mechanical properties can be modulated by adjusting their geometric arrangement without compromising porosity [11].

Tissue Engineering.

The development of scaffolds for tissue engineering has been widely investigated to prepare a 3D structure which will mimic the function of natural extracellular matrix into which cells can be seeded and proliferate [4, 12-14]. Many of these workers have investigated methods to fabricate scaffolds for bone replacement and fracture healing [15, 16]. In this case, the scaffold needs to perfectly match the defect site within the patient's body. Medical imaging technologies are typically used to gather implant site external geometric data.

Methods for this included, among others, computer tomography (CT) and Magnetic Resonance Imagining (MRI). Collected data can then be used to design the custom scaffold structure. There are two main techniques used to design the internal scaffold geometry. Micro-CT scanned internal bone structures of donor samples can be recorded and attempts made to replicate these directly [17]. This has limited applicability currently as scanned trabecular structures are complex and hard to fabricate with current technologies [21]. The second method for scaffold internal structure determination is to generate CAD files with predefined geometric basis and assess these for adequate mechanical performance and ability to fabricate [18, 19]. This ability to tailor scaffold performance allows different scaffold structures to be generated for specific locations within the body which often have very different mechanical requirements [16, 20].

Scaffold Manufacturing Techniques.

One of the challenges in context of bone scaffolds is provision of a suitable manufacturing process. Rapid prototyping (RP) techniques that are used for scaffold fabrication include fused deposition modelling (FDM), selective laser sintering (SLS), stereolithography (SLA) and direct 3D printing (3DP). General limitations of these include the low level of dimensional accuracy and structural complexity achievable, the lack of available materials which may be used, and the relatively weak mechanical properties achievable compared to conventional processing. In all of these techniques, the scaffold is built in an additive manner with each 2D slice bonded layer by layer to previous slice to build up the final structure. In these processes, dimensional accuracy is among other parameters limited by the nozzle diameter, laser spot diameter and powder particle size. Table 1 shows resolutions currently achievable by SLA, FDM and 3DP rapid prototyping systems.

Fabrication method	**Resolution [mm]**
Stereolitography	0.0762 x,y-direction 0.0508 z-direction
Fused deposition modelling	0.0762 x,y-direction 0.013 z-direction
3D plotting	0.05 x,y,z-direction

Table 1: Achievable resolutions of currently available rapid prototyping systems [21]

Structural Requirements of Scaffolds.

The osteoconductivity of the scaffold is a crucial factor in the tissue regeneration process. In particular, the internal architecture plays an important role in determining the rate and degree of bone ingrowth [22-24]. It is necessary to remember that apart from mechanical properties and strength during the healing process, the scaffold must also support a quick and efficient healing process. To achieve these goals the pore size must be large enough to allow free nutrient and osteoblast transport but small enough to ensure adequate mechanical properties [25]. Two commonly studied parameters are pore size and interconnectivity. Larger sized micro-porosity (above 100 p.m) is thought to contribute to osteogenesis by facilitating cell and ion transport while smaller ranged micro-porosity (less than 60 μm) may improve bone growth into scaffolds by increasing surface area for protein adsorption, increasing ionic solubility in the micro-environment and providing attachment points for osteoblasts [17]. Taking into account, that designed scaffolds also need to be manufacturable, the challenge of scaffold geometry optimisation is a fundamental problem to be solved in tissue development.

Materials and Methods

CAD Files Generation. In order to simulate the reactions of trabecular bone architecture to physiological loading conditions three different scaffold unit cell geometries were design using Solid Edge software (Siemens Product Lifecycle Management Software Inc., Siemens AG, Munich, Germany). These unit cells were of cubic, triangular and hexagonal geometry. The macrostructure models were built from repeated stacking of these unit cells. Figure 1 shows the 3D view and 2D

cross section of the unit cells used. Each structure was built with cylindrical struts. Three pore sizes 120, 340 and 600[im and porosity values 30%, 50% and 70% were investigated. These were developed in the macrostructure models by altering the strut thickness and number of repeating unit cells. The pore size was measured as the largest diameter of circle which would fit within the plan view unit cell void, see Figure 1 (b), (d), and (f). Table 2 shows the various volumes and numbers of repeated unit cells used in order to achieve the required porosity levels and pore sizes. The emboldened numbers represent the external geometrical dimensions in millimetres of each of the scaffolds. The boundary box was then filled with the pre-designed structures. From this table it can also be seen that nine macrostructures were developed for each of the three unit cell geometries resulting in 27 geometries that were first analysed for stress and strain distribution with ANSYS (ANSYS Inc., Canonsburg, PA) finite element software. A further 27 experiments were performed with a solid loading block physically attached to the top and bottom of the macrostructures used for the first 27 experiments. The height of each loading block was set as 40% of the total height of the scaffold in order to provide uniform stress accommodation at the loading block-scaffold interface and hence reduction of end-effects [26]. These latter tests were performed in order to simulate a cortical multilayered structure and examine the effect of stress deployment across the loading surface on stress distribution within the scaffold. The loading conditions for the cubic structure with and without loading blocks are shown in Figure 2. The bottom surfaces were constrained and the loading was applied uniformly across the top surface. Similar loading conditions were applied for all models presented in this paper. A pressure level of 5.51 kPa and a loading direction along the y-axis were chosen with respect

to the unit cells shown in Figure 1 (b), (d), and (1). These applied loading conditions were chosen to simulate in-vivo loading conditions [26].

Pore size, µm / Porosity, %	120	340	600	Number of unit cells for cubic structure	Number of unit cells for hexagonal structure	Number of unit cells for triangular structure
30	**2 x 2 x 2**	**5.7 x 5.7 x 5.7**	**10 x 10 x 10**	5x5x5	5x5x6	5x5x5
50	**2 x 2 x 2**	**5.7 x 5.7 x 5.7**	**10 x 10 x 10**	7x7x7	7x7x8	6x7x7
70	**2 x 2 x 2**	**5.7 x 5.7 x 5.7**	**10 x 10 x 10**	10x10x10	12x12x13	8x10x10

Table 2: Variation of cell dimensions in millimetres (emboldened) and number of unit cell repetitions for the chosen pore sizes and porosity levels

FEA Set Up. The stress and strain distribution and maximum stress values in the meshed scaffold architectures were analysed with ANSYS Workbench 11.0 linear finite element analysis software. The equivalent (von-Mises) elastic stress and strain were evaluated and documented for each of the 54 designed architectures. Each structure was meshed with a different number of tetrahedron elements. More complex structures required more elements for accurate meshing. Table 3 shows the number of tetrahedron elements for each of the scaffolds. This table presents the results from error convergence analysis which conducted to ensure that the number of elements used was sufficient for reliable finite element result calculation. It can be seen that the more complex the shape, the larger the number of elements that were required for accurate meshing. In order to ensure accurate meshing of the geometries, size controls and shape refinement options within ANSYS were also used. For the material properties of the scaffold struts, the properties ofO020cortical bone were used. Accordingly to the data known from previous work, the Young's modulus value was set to 18.3 GPa, the material density to 1810 kg/m^3, and Poisson's ratio to 0.28 [27, 28].

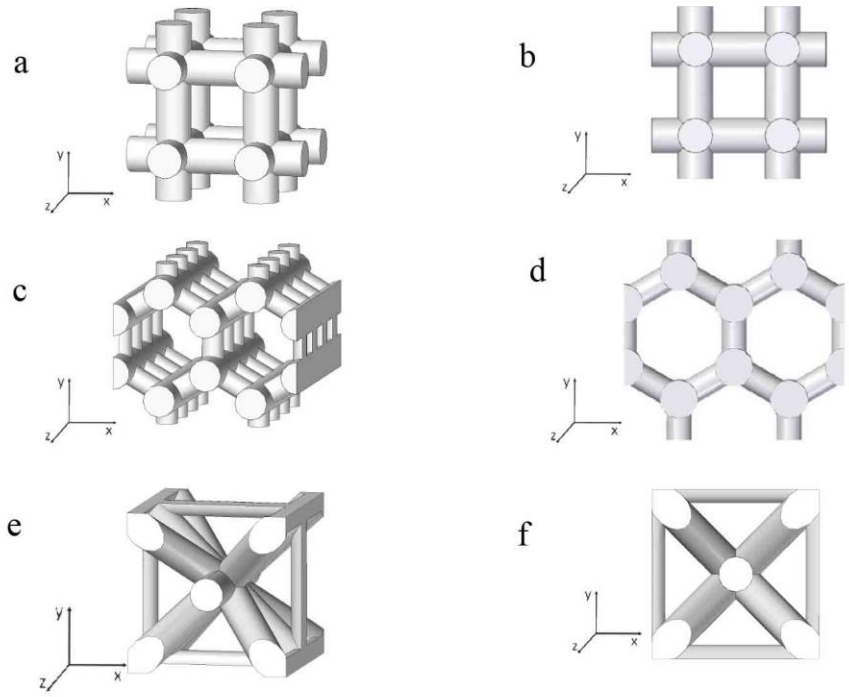

Figure 1: Geometrical representation of designed structures. 3D view of (a) cubic, (c) triangular and (e) hexagonal unit cell and 2D plan view of (b) cubic, (d) triangular and (f) hexagonal unit cell structures

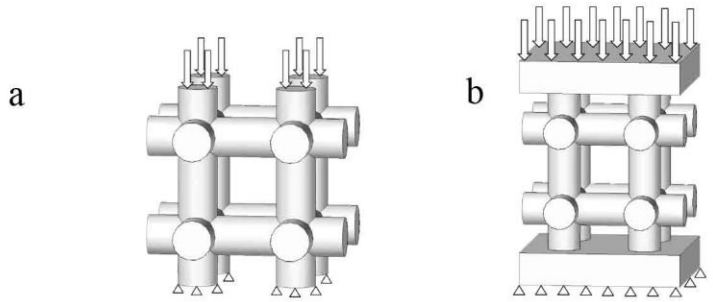

Figure 2: Schematic of the loading conditions set for the scaffolds (a) without loading blocks and (b) with loading blocks

Porosity	**Cubic**			**Hexagonal**			**Triangular**		
	120µm	340µm	600µm	120µm	340µm	600µm	120µm	340µm	600µm
30%	12 271	12 245	12 296	35 029	37 008	35 688	114 689	96 963	114 821
50%	27 248	27 554	27 439	78 940	80 847	80 218	350 084	352 479	354 728
70%	71 976	72 374	72 382	658 265	659 328	65 8585	1 076 301	1 083 523	1 089 343

Table 2: Number of elements for each series of the scaffold with no loading block

Results

Initial tests confirmed that the loading block significantly changed the stress distribution within the scaffold. The maximum stresses recorded for the cubic-based structures when loading blocks were used were on average 5% higher than those recorded when no loading blocks were applied

The maximum stress values recorded in cubic macrostructure with and without loading block are shown in Figure 3. On the other hand, for the triangular and hexagonal based architecture the maximum stresses recorded when loading blocks were used were lower (by approximately 32% and 24% respectively) than that found compared to when no loading blocks were applied.

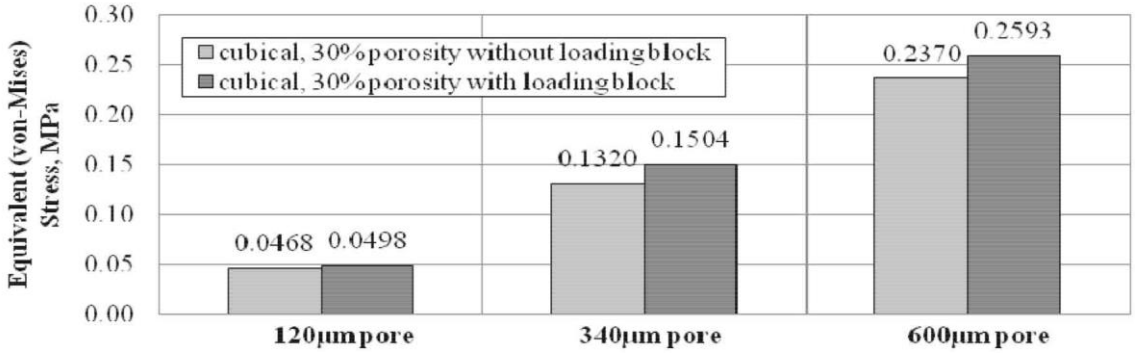

Figure 3: Maximum stress values for cubic structures with and without loading block at pore sizes of 120, 340 and 600 µm

Results for structures where loading blocks were not used demonstrated that the highest stress concentration occur on the top or the bottom. Different stress distributions and locations of highest stressed points for the hexagonal based structure with loading and no-loading blocks are shown in Figure 4. Applying loads through the loading blocks produced a more even stress distribution through the scaffold with the maximum stress occurring somewhere centrally within the scaffold. The highest stress value for all of the structures examined was 1.48 MPa. This occurred for the hexagonal structure with pore size of 600μm and 70% porosity. The results showed that larger stress levels were recorded at the surface of struts than in their centre. The maximum stress values recorded for structures with loading blocks, pore sizes of 120, 340 and 600μm and with a porosity level of 30% are shown in Figure 5. Corresponding maximum stress values for porosity levels of 50% and 70% are shown in Figures 6 and 7 respectively. It is evident from these results that in general as the pore sizes increase for a given structure and porosity level, the maximum stress values also increase. The only exception to this was for the 70% porous cubic structure. The largest stress for 30% porosity level was found in the triangular based structure, see Figure 5. This was approximately three times higher than that seen in the other structures. A general trend of increasing maximum stress levels was observed as the porosity levels were increased from 30% to 70%. Looking specifically at the cubic structures an increase in the average maximum stress level of 28% was recorded as the porosity level was raised from 30% to 50%, see Figure 5 and 6. An average increase in maximum stress of 140% was also recorded between

50% and 70% porosity levels, see Figure 6 and 7. This result is as would be expected due to the reduced level of solid supporting structure at the higher porosity levels.

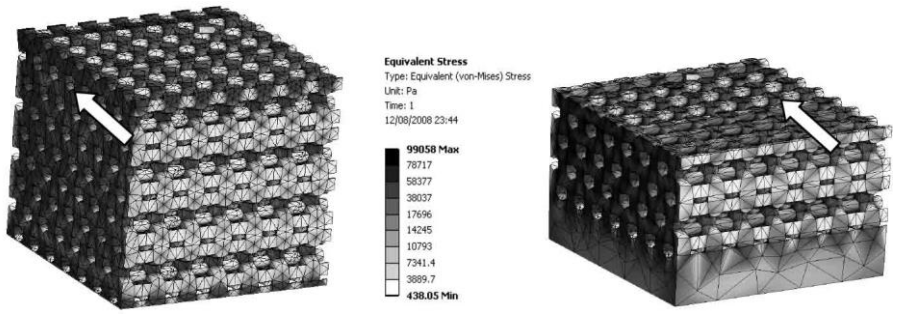

Figure 4: Von-Mises stress distribution for (a) hexagonal structure, with 50% porosity without loading block, and (b) cross section of hexagonal structure with the maximum stress value recorded centrally with the use of loading block. Arrows indicate the points of maximum stress

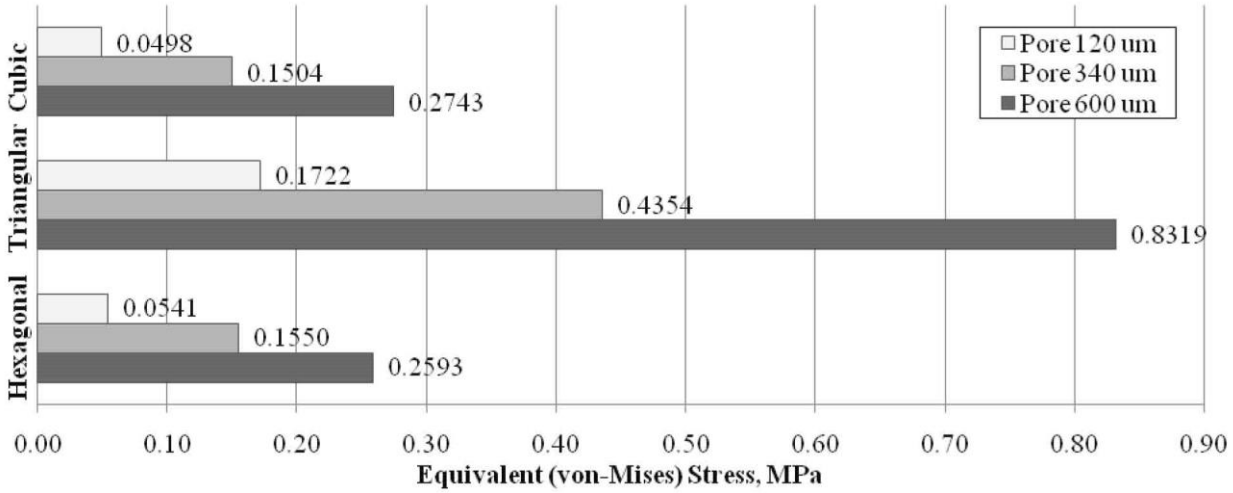

Figure 5: Equivalent (von-Mises) Stress for 30% porosity scaffolds

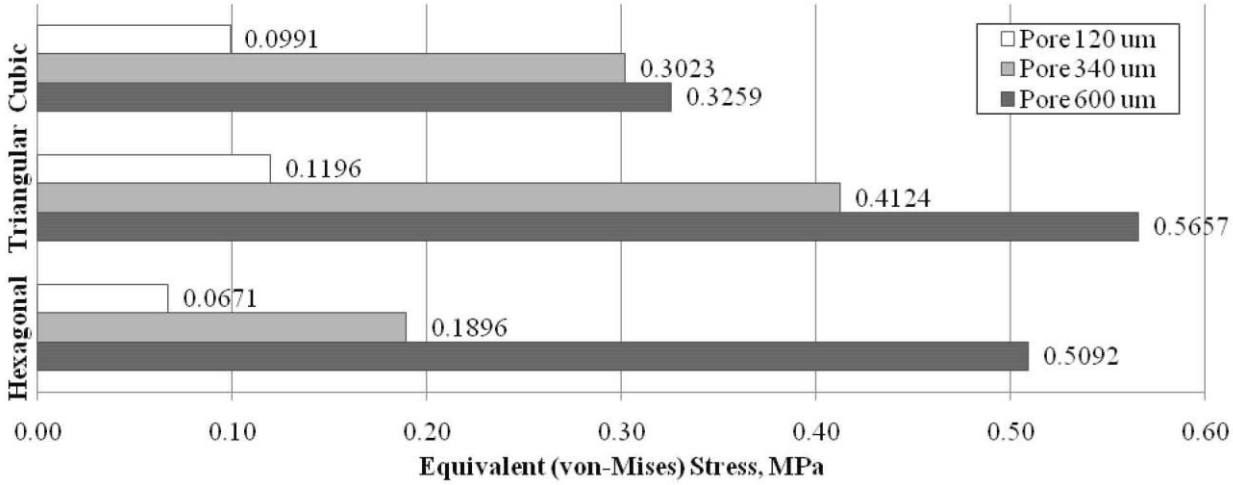

Figure 6: Equivalent (von-Mises) Stress for 50% porosity scaffolds

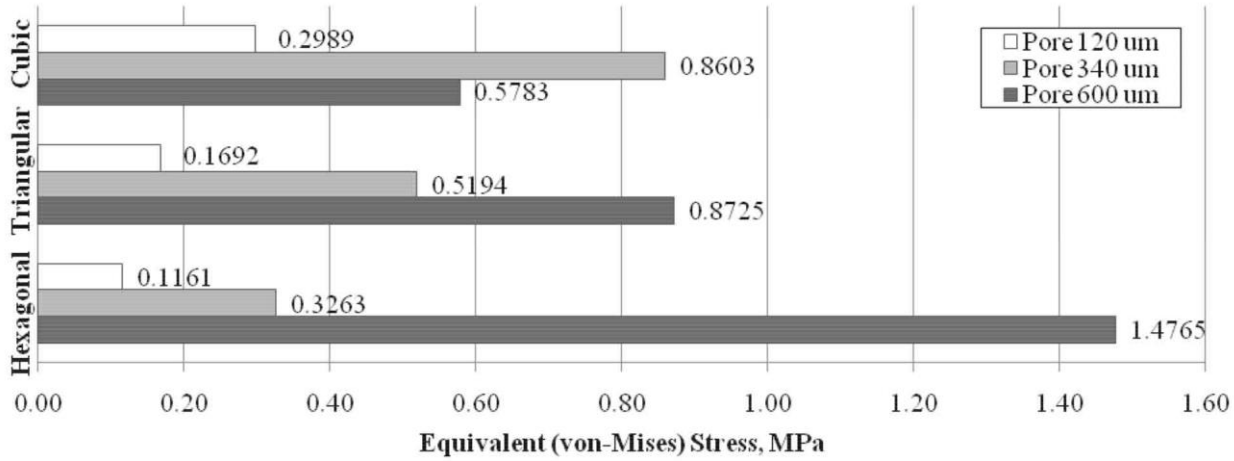

Figure 7: Equivalent (von-Mises) Stress for 70% porosity scaffolds

Conclusions

In this study, we generated and tested three different scaffold geometries. Mechanical properties were seen to depend on the designed pore shape (architecture), pore size (120, 340 and 600 μm) and loading conditions (with or without loading blocks). Examination of these parameter variations on 8mm3, 22.7mm3 and 1000mm3 porous scaffolds were conducted to fully examine their influence on stress distribution. The work presented in this paper suggests that the geometrical design of the structure plays a significant role in the stress distribution and highlights the great possibilities for scaffold design to enhance bone regeneration. Studies have shown, that higher values of stress located on the surface of struts within the scaffold can enhance the bone remodelling process.

The finite element analysis results presented in this paper show that mechanical properties and stress and strain distribution within the scaffold strongly depend on the porosity of the designed structure. Overall the pore size was seen to be more important than the porosity level in determining the overall maximum stress level. The porosity level however is also important in determining the osteoconductivity of the scaffold structure. By increasing the porosity levels from 30% to 70% with the same pore sizes, the maximum stress values increased dramatically. The pore size of the scaffold is also important for the fabrication method. To date all of the rapid prototyping methods have certain limitations. More complicated and smaller structures may often not be manufactured. Most of these technologies are not nominally currently capable of consistent production of pores sizes below 500μm. The results for the 600μm pore size in this work are therefore most relevant to the manufacturing capabilities of current rapid manufacturing technologies.

The hexagonal structure presented in this paper, although examined in only one direction, would be the most anisotropic structure relative to the cubic and triangular based structures. The cubic and triangular structures are relatively isotropic compared to the hexagonal structure. Previous work shows, that mechanical properties may vary if the scaffold is loaded from different directions. Anisotropy is important in considering the osteoconductivity of designed scaffolds. Stress distribution and pore size location affect the remodelling processes and different loading conditions may change the maximum stress values and its location. The dominant loading direction should encourage pore sizes and distribution to allow cells growth into the larger pores as well as providing nutrients and building material [9].

Another interesting finding from this work from examination of the strut cross sectional stress distribution was that larger values of stress were recorded at the surface of the struts

compared to the centres. In this work the pore size, porosity level and loading methods have been shown to be strongly correlated with the stress levels experienced in the structures. These findings indicated the ability to design a strut architecture within which the stress levels can be varied to a larger degree at the strut surfaces such that cellular attachment and growth can be promoted.

Acknowledgments

This research has been supported by a Marie Curie Early Stage Research Training Fellowship of the European Community's Sixth Framework Programme under contract number MEST-CT-2005- 020621 .

References

[1] P. Lal, and W. Sun, Computer modeling approach for microsphere-packed bone scaffold, Computer-Aided Design, vol. 36 (2004), 487-497.
[2] B. Starly, W. Lau, T. Bradbury, and W. Sun, Internal architecture design and freeform fabrication of tissue replacement structures, Computer-Aided Design, vol. 38 (2006), 115-124.
[3] M.J. Mondrinos, R. Dembzynski, L. Lu, V.K.C. Byrapogu, D.M. Wootton, P.I. Lelkes, and J. Zhou, Porogen-based solid freeform fabrication of polycaprolactone-calcium phosphate scaffolds for tissue engineering, Biomaterials, vol. 27 (2006), 4399-4408.
[4] K.F. Leong, C.K. Chua, N. Sudarmadji, and W.Y. Yeong, Engineering functionally graded tissue engineering scaffolds, Journal of the Mechanical Behavior of Biomedical Materials, vol. 1 (2008), 140-152.
[5] E. Saiz, L. Gremillard, G. Menendez, P. Miranda, K. Gryn, and A.P. Tomsia, Preparation of porous hydroxyapatite scaffolds, Materials Science and Engineering: C, vol. 27 (2007), 546-550. [6] L. Liulan, H. Qingxi, H. Xianxu, and X. Gaochun, Design and Fabrication of Bone Tissue Engineering Scaffolds via Rapid Prototyping and CAD, Journal of Rare Earths, vol. 25 (2007), 379-383.
[7] B.-S. Kim, and D.J. Mooney, Development of biocompatible synthetic extracellular matrices for tissue engineering, Trends in Biotechnology, vol. 16 (1998), 224-230.
[8] W.-Y. Yeong, C.-K. Chua, K.-F. Leong, and M. Chandrasekaran, Rapid prototyping in tissue engineering: challenges and potential, Trends in Biotechnology, vol. 22 (2004), 643-652.
[9] C. Qu, Q.-H. Qin, and Y. Kang, A hypothetical mechanism of bone remodeling and modeling under electromagnetic loads, Biomaterials, vol. 27 (2006), 4050-4057.
[10] S. Tayyar, P.S. Weinhold, R.A. Butler, J.C. Woodard, L.D. Zardiackas, K.R. St. John, J.M. Bledsoe, and J.A. Gilbert, Computer simulation of trabecular remodeling using a simplified structural model, Bone, vol. 25 (1999), 733-739.
[11] M. Charles-Harris, S. del Valle, E. Hentges, P. Bleuet, D. Lacroix, and J.A. Planell, Mechanical and structural characterisation of completely degradable polylactic acid/calcium phosphate glass scaffolds, Biomaterials, vol. 28 (2007), 4429-4438.
[12] W. Helen, and J.E. Gough, Cell viability, proliferation and extracellular matrix production of human annulus fibrosus cells cultured within PDLLA/Bioglass® composite foam scaffolds in vitro, Acta Biomaterialia, vol. 4 (2008), 230-243.
[13] Y. Zhang, Y. Wang, B. Shi, and X. Cheng, A platelet-derived growth factor releasing chitosan/coral composite scaffold for periodontal tissue engineering, Biomaterials, vol. 28 (2007), 1515-1522.

[14] H.H. Xu, and C.G. Simon, Fast setting calcium phosphate-chitosan scaffold: mechanical properties and biocompatibility, Biomaterials, vol. 26 (2005), 1337-1348.
[15] P. Giannoudis, C. Tzioupis, T. Almalki, and R. Buckley, Fracture healing in osteoporotic fractures: Is it really different?: A basic science perspective, Scientific basis of fracture healing: an update, vol. 38 (2007), S90-S99.
[16] D. Lacroix, and P.J. Prendergast, A mechano-regulation model for tissue differentiation during fracture healing: analysis of gap size and loading, Journal of Biomechanics, vol. 35 (2002), 1163-1171
[17] Z. Wu, W. Lei, Y. Hu, H. Wang, S. Wan, Z. Ma, H. Sang, S. Fu, and Y. Han, Effect of ovariectomy on BMD, micro-architecture and biomechanics of cortical and cancellous bones in a sheep model, Medical Engineering & Physics, vol. In Press, Corrected Proof
[18] B.C. Tellis, J.A. Szivek, C.L. Bliss, D.S. Margolis, R.K. Vaidyanathan, and P. Calvert, Trabecular scaffolds created using micro CT guided fused deposition modeling, Materials Science and Engineering: C, vol. 28 (2008), 171-178.
[19] G.E. Ryan, A.S. Pandit, and D.P. Apatsidis, Porous titanium scaffolds fabricated using a rapid prototyping and powder metallurgy technique, Biomaterials, vol. 29 (2008), 3625-3635.
[20] A.S. Lin, T.H. Barrows, S.H. Cartmell, and R.E. Guldberg, Microarchitectural and mechanical characterization of oriented porous polymer scaffolds, Biomaterials, vol. 24 (2003), 481-489.
[21] M. Wettergreen, B. Bucklen, W. Sun, and M. Liebschner, Computer-Aided Tissue Engineering of a Human Vertebral Body, Annals of Biomedical Engineering, vol. 33 (2005), 1333-1343.
[22] A.C. Jones, C.H. Arns, A.P. Sheppard, D.W. Hutmacher, B.K. Milthorpe, and M.A. Knackstedt, Assessment of bone ingrowth into porous biomaterials using MICRO-CT, Biomaterials, vol. 28 (2007), 2491-2504.
[23] J.R. Woodard, A.J. Hilldore, S.K. Lan, C.J. Park, A.W. Morgan, J.A.C. Eurell, S.G. Clark, M.B. Wheeler, R.D. Jamison, and A.J. Wagoner Johnson, The mechanical properties and osteoconductivity of hydroxyapatite bone scaffolds with multi-scale porosity, Biomaterials, vol. 28 (2007), 45-54.
[24] V. Karageorgiou, and D. Kaplan, Porosity of 3D biomaterial scaffolds and osteogenesis, Biomaterials, vol. 26 (2005), 5474-5491.
[25] S. Bose, J. Darsell, M. Kintner, H. Hosick, and A. Bandyopadhyay, Pore size and pore volume effects on alumina and TCP ceramic scaffolds, Materials Science and Engineering: C, vol. 23 (2003), 479-486.
[26] P. Mc Donnell, M.A. Liebschner, W. Tawackoli, and P.E. Mc Hugh, Vibrational testing of trabecular bone architectures using rapid prototype models, Medical Engineering & Physics, vol. In Press, Corrected Proof.
[27] X.J. Wang, X.B. Chen, P.D. Hodgson, and C.E. Wen, Elastic modulus and hardness of cortical and trabecular bovine bone measured by nanoindentation, Transactions of Nonferrous Metals Society of China, vol. 16 (2006), s744-s748.
[28] J.Y. Rho, R.B. Ashman, and C.H. Turner, Young's modulus of trabecular and cortical bone material: Ultrasonic and microtensile measurements, Journal of Biomechanics, vol. 26 (1993), 111-119.